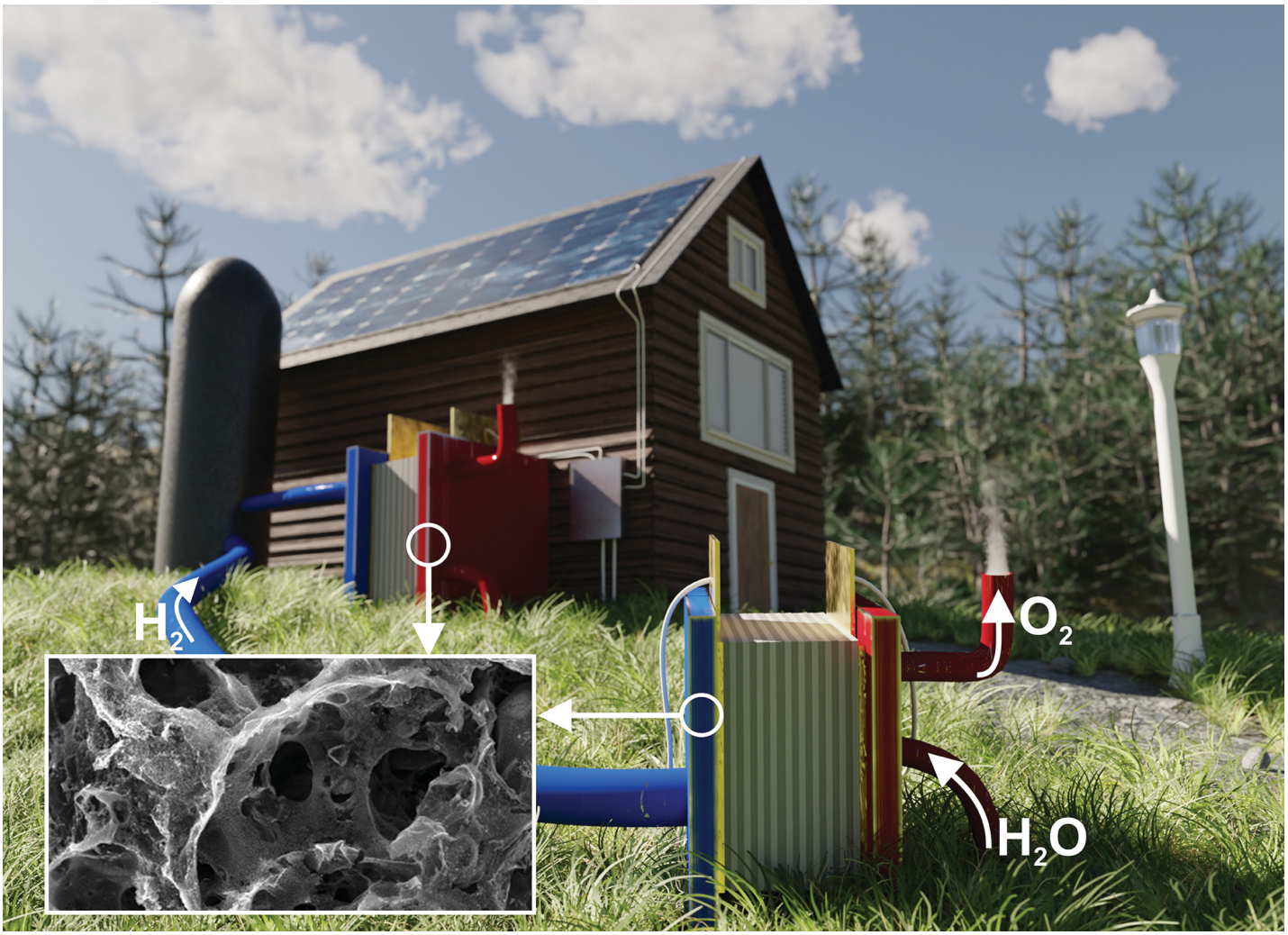

Showcasing research from the group of Assoc. Prof. Eduardo Gracia-Espino at Umeå University, Sweden.

Scalable production of foam-like nickel–molybdenum coatings *via* plasma spraying as bifunctional electrocatalysts for water splitting

This work investigates the scalable production of foam-like nanostructured Ni–Mo coatings containing the highly active Ni_4Mo *via* atmospheric plasma spraying. The Ni–Mo coatings exhibit high activity towards both hydrogen evolution and oxygen evolution reactions in alkaline media. Large-area electrodes are produced in seconds with variable material loading without compromising the foam-like structure. Theoretical activity maps reveal that Ni_4Mo exhibit reduced hydrogen adsorption energies and enhanced water dissociation which ultimately results in improved catalytic activity.

As featured in:

See Eduardo Gracia-Espino *et al.*, *Phys. Chem. Chem. Phys.*, 2023, **25**, 20794.

ROYAL SOCIETY OF CHEMISTRY

rsc.li/pccp

Registered charity number: 207890

PCCP Owner Societies

PCCP

PAPER

View Article Online
View Journal | View Issue

Open Access Article. Published on 07 July 2023. Downloaded on 1/22/2026 5:08:32 PM.
This article is licensed under a Creative Commons Attribution 3.0 Unported Licence.

Check for updates

Cite this: *Phys. Chem. Chem. Phys.*, 2023, **25**, 20794

Scalable production of foam-like nickel–molybdenum coatings *via* plasma spraying as bifunctional electrocatalysts for water splitting†

Xiuyu Wu, Alexis Piñeiro-García, Mouna Rafei, Nicolas Boulanger, Esdras Josué Canto-Aguilar and Eduardo Gracia-Espino*

Received 30th March 2023,
Accepted 12th June 2023

DOI: 10.1039/d3cp01444d

rsc.li/pccp

Foam-like NiMo coatings were produced from an inexpensive mixture of Ni, Al, and Mo powders *via* atmospheric plasma spraying. The coatings were deposited onto stainless-steel meshes forming a highly porous network mainly composed of nanostructured Ni and highly active Ni_4Mo. High material loading (200 mg cm^{-2}) with large surface area (1769 cm^2 per cm^2) was achieved without compromising the foam-like characteristics. The coatings exhibited excellent activity towards both hydrogen evolution (HER) and oxygen evolution (OER) reactions in alkaline media. The HER active coating required an overpotential of 42 mV to reach a current density of −50 mA cm^{-2} with minimum degradation after a 24 h chronoamperometry test at −10 mA cm^{-2}. Theoretical simulations showed that several crystal surfaces of Ni_4Mo exhibit near optimum hydrogen adsorption energies and improved water dissociation that benefit the HER activity. The OER active coating also consisting of nanostructured Ni and Ni_4Mo required only 310 mV to achieve a current density of 50 mA cm^{-2}. The OER activity was maintained even after 48 h of continuous operation. We envisage that the development of scalable production techniques for Ni_4Mo alloys will greatly benefit its usage in commercial alkaline water electrolysers.

Introduction

Nowadays, alkaline water electrolysers can reach efficiencies of ∼70%, where nickel plays a key role due to its good electrochemical activity and stability.[1–3] However, Ni exhibits a strong hydrogen adsorption energy, resulting in large overpotentials for the hydrogen evolution reaction (HER).[4] Therefore, decreasing its interaction strength with hydrogen is a key parameter that is currently being investigated. Alloying Ni with other transition metals such as Fe, Co, and Mo has been a successful strategy to improve its catalytic activity.[5–10] Previous studies have shown that nickel-based binary and ternary alloys containing Mo have great potential for the HER in alkaline media,[10–12] where among the most active electrocatalysts reported in recent years is tetragonal Ni_4Mo.[9,11,12] The high activity of Ni_4Mo has been attributed to its band structure that mimics Pt.[9] Ni–Mo nanostructures are commonly fabricated by electrochemical deposition,[7,8] a hydrothermal method,[9,11,13] and chemical vapor deposition,[14] where typically, multi-step synthesis is used to achieve large-surface-area nanostructures. For example, Zhou, Y., and co-workers reported the production of highly porous Ni_4Mo *via* a hydrothermal process, followed by thermal annealing in a H_2 atmosphere.[9] In a similar process, Zhang, J. *et al.* produced Ni_4Mo nanoparticles onto MoO_2 cuboids deposited onto nickel foam.[11] Xiao, J. used a carbon fiber array covered with carbon tubes, which are then covered with Ni_4Mo sheets.[12] Finally, Ding, H. *et al.* used nitrogen-doped graphene foam as a substrate for NiMo nanosheets.[13] These works highlight the advantage of hierarchical structures where a large surface area and excellent catalytic performance are observed, but these approaches ultimately complicate the material production and limit their large-scale production.

Therefore, in this study, we report the scalable production of Ni–Mo coatings containing highly active Ni_4Mo onto stainless-steel meshes *via* atmospheric plasma spraying. A foam-like structure was obtained, where nanostructured Ni and Ni_4Mo are dominant crystal phases, resulting in high electrochemical activity towards both HER and OER in alkaline media. Large-area electrodes were produced in just 30 s with variable material loading without compromising the foam-like structure. Theoretical activity maps reveal that diverse crystal surfaces of Ni_4Mo exhibit reduced hydrogen adsorption energy and improved water dissociation, contributing directly to the HER activity.

Department of Physics, Umeå University, SE-901 87 Umeå, Sweden.
E-mail: eduardo.gracia@umu.se

† Electronic supplementary information (ESI) available. See DOI: https://doi.org/10.1039/d3cp01444d

 This journal is © the Owner Societies 2023

Open Access Article. Published on 07 July 2023. Downloaded on 1/22/2026 5:08:32 PM.
This article is licensed under a Creative Commons Attribution 3.0 Unported Licence.

Experimental section

Electrode preparation

NiAlMo electrodes were produced by atmospheric plasma spraying (APS). An APS (Metallisation, Met-PCC(PLAS)) equipment fitted with a PL50 pistol and a 6 mm nozzle was used. Ar and N_2 were used as primary and secondary gases, respectively. The precursor material is a uniform powder (Metallisation 99627/16 – P627) mixture of individual Ni, Al, and Mo metals with a composition of 89.5, 5.5, and 5.0 wt%, respectively, and particle size ranging from 45–90 μm. The powder was injected into the plasma plume *via* an external nozzle with the use of a volumetric feeder with a disk rotation speed of 20 rpm and 8.0 NL min^{-1} of N_2 as a gas carrier. Stainless-steel meshes (SS316) with a sieve size of 150 μm were used as a substrate. The steel meshes were cleaned in an ultrasonic bath with a mixture of deionized water and ethanol (50 : 50) for 30 min. The power used during the coating process was varied (16, 17, 20, 24, and 38 kW) by modifying the flow and ratio of the primary and secondary gases and the electrical current used to generate the plasma, see Table S1 in the ESI.† A robotic arm (ABB 2600) was used to manipulate the plasma torch. A raster spraying pattern with a lateral velocity of 250 mm s^{-1} and a vertical displacement of 4 mm per turn was employed. 13 cycles were used to cover an area of 20 cm × 22 cm; the steel mesh substrate (7 cm × 5 cm) was collocated at the centre to assure a homogeneous coating. The final coating was achieved by applying a total of 5 layers on the substrate; these samples were labelled NiAlMo. After spraying, a sample of size 3 cm × 5 cm was immersed in a 30 wt% KOH and10 wt% K–Na–tartrate–tetrahydrate (Sigma-Aldrich) solution (50 mL) for 24 h at 80 °C to partially remove Al. After Al leaching, the samples were stored in Ar-saturated DI water; these are labelled NiMo.

Material characterization

X-ray diffraction (XRD) studies were carried out on a PANalytical X'pert diffractometer (λ = 1.5406 Å, Cu Kα) within the range of 5 to 80 degrees (a step size of 0.01395° with 0.5 s per step) under ambient conditions. Scanning electron microscopy (SEM) studies were performed on a Carl Zeiss Merlin equipped with energy dispersive X-ray spectroscopy (EDS). X-ray photoelectron spectroscopy (XPS) analyses were conducted on a Kratos Axis Ultra DLD electro-spectrometer equipped with a monochromatic X-ray source (an Al K line of 1486.6 eV).

Electrochemical characterization

The electrochemical studies were performed using a potentiostat (Ivium Technologies) in a three-electrode cell filled with Ar-saturated 1 M KOH electrolyte at room temperature. Ag/AgCl (3 M KCl) and a graphite rod were used as the reference and counter electrodes, respectively. The working electrode consisted of the activated (Al leached) NiMo coating with an area of 1 cm^2; the electrical contact was made through the stainless-steel mesh with crocodile clips. The catalytic activity was measured by cyclic voltammetry (CV) in the range of −1.036 to −1.236 V *vs.* Ag/AgCl for HER (scan rate of 5 mV s^{-1}) and 0.194 to 0.594 V *vs.* Ag/AgCl for OER (1 mV s^{-1}). A total of 9 (30) CV cycles were used for HER (OER) to achieve a stable polarization curve, and the last cathodic (anodic) scan was used in this work. The measured potential was converted to the reversible hydrogen electrode (RHE) potential by using the Nernst equation, $E_{RHE} = E_{Cell} + 0.059pH + E_{Ag/AgCl}$; $E_{Ag/AgCl}$ = 0.210 V *vs.* SHE, where E_{Cell} is the experimental measured potential. The *iR* compensation was performed by subtracting 90% of the voltage drop caused by the Ohmic resistance (R_Ω) obtained from EIS studies using the expression $E_{iR\text{-free}} = E_{\text{measured}(vs.\ \text{RHE})} - 0.90 \cdot iR_\Omega$.

Electrochemical impedance spectroscopy (EIS) was performed at 0 V (*vs.* RHE) with an amplitude of 10 mV in the frequency range of 10 kHz to 0.1 Hz for the NiMo sample sprayed at 20 kW at 100 mm and 10 kHz to 0.01 Hz for all other samples deposited at 20 kW. Detailed sample labels and spraying conditions are listed in Table S1 (ESI†). The operational stability was evaluated by applying 1000 CV cycles from −0.15 to 0.05 V (*vs.* RHE) for HER and from 1.0 to 1.6 V (*vs.* RHE) for OER at a scan rate of 50 mV s^{-1}. A subsequent chronoamperometric (CA) study was carried out at a constant potential to achieve a current density of −10 mA cm^{-2} for HER for 24 h. For OER, two CA studies were conducted at 10 and 50 mA cm^{-2} for 24 and 48 h, respectively. The double-layer capacitance (C_{dl}) of NiMo electrodes was evaluated by a series of CV studies at different scan rates (5 to 100 mV s^{-1}) at ±50 mV of the open-circuit potential.[15,16]

The double-layer capacitance was determined in a non-aqueous electrolyte by CV experiments in a conventional three-electrode electrochemical cell, using the NiMo coatings on stainless-steel meshes as working electrodes, 0.1 M NBu_4PF_6 (Sigma-Aldrich, ≥99.0%) prepared in CH_3CN (Fisher scientific, 99.99%) electrolyte as the working solution, Pt wire as the counter electrode, and Ag/Ag^+ (0.1 NBu_4PF_6 with 0.01 M $AgNO_3$, Sigma-Aldrich, ≥99.8%) as the reference electrode (0.54 V *vs.* NHE).[17] Before any measurement, the reference electrode was calibrated *versus* the Fc/Fc^+ redox couple (0.63 V *vs.* NHE)[18] using a solution 0.1 M NBu_4PF_6 with 1.0 mM of ferrocene (Sigma-Aldrich, 98.0%) in CH_3CN. All the working electrodes were cycled at different scan rates (5 to 100 mV s^{-1}) in the potential window of −0.43 to −0.22 V *vs.* Ag/Ag^+ (0.01 M) at 20 °C under an Ar atmosphere.

Computational details

The adsorption free energy of hydrogen (ΔG_H) was evaluated using the computational hydrogen–electrode model using the relation $\Delta G_H = \Delta E_H + \Delta E_{ZPE} - T\Delta S$,[4,19,20] where ΔE_H is the hydrogen adsorption energy using a H_2 molecule as the reference state. The term ($\Delta E_{ZPE} - T\Delta S$) involving the zero-point energy and entropy contributions has been previously estimated for metallic surfaces to be 0.24 eV;[19] this value is used in our calculations. ΔG_H was evaluated at high hydrogen coverage as expected for Ni-based alloys.[4] The computations were performed using density functional theory (DFT) as implemented in the SIESTA code.[21] A double-ζ polarized basis was used to represent the valence electrons, and an energy cut-off of 350 Ry was used for charge and potential integration. A *K*-grid of 6 × 6 × 1 was used to sample the Brillouin zone of the Ni_4Mo slabs. All systems were relaxed using conjugate gradient minimization until the

Open Access Article. Published on 07 July 2023. Downloaded on 1/22/2026 5:08:32 PM.
This article is licensed under a Creative Commons Attribution 3.0 Unported Licence.

maximum forces were <0.04 eV Å^{-1}. The bottom three layers of the metal slabs were kept fixed during optimization. The dissociation energy (E_{diss}) of water was evaluated using $E_{diss} = E_{H\text{-}OH\text{-}surf} - E_{H_2O\text{-}surf}$, where $E_{H\text{-}OH\text{-}surf}$ ($E_{H_2O\text{-}surf}$) is the energy of the H and OH intermediates (H_2O) adsorbed onto the metal surface.

Results and discussion

Characteristics of nickel–molybdenum coatings

The fabrication process of the initial metallic NiAlMo coating was performed by APS using a metallic powder precursor of individual Ni, Al, and Mo (particle size 45–90 μm, not alloyed), as illustrated in Fig. 1(a). The powder is injected into the plasma plume *via* an external nozzle located just outside the anode. A robotic arm is used to manipulate the plasma torch, and the coating is carried out using a raster spraying pattern where the entire substrate area (35 cm^2) was coated in ∼30 seconds. This process was repeated 5 times to increase the coating thickness, see the experimental section for further details. The resulting coatings were robust and easy to handle. Afterwards, the coatings were treated in an alkaline solution to partially remove aluminium and increase their porosity and surface area (Fig. 1(b)).[22–24]

Before performing Al leaching, we carried out a series of XRD studies to identify how the spraying distance and power affected the constituents and catalytic activity of the as-sprayed NiAlMo coatings. As a first optimization step, we kept the spraying distance (distance between the nozzle and the substrate) constant at 250 mm and then we prepared coatings using 20, 24, and 38 kW. Afterwards, a second optimization step was performed by varying the spraying distance (100, 200, 250, and 300 mm away from the substrate) while maintaining the power at 20 kW (spraying conditions and sample labels are listed in Table S1, ESI†). The selection of the power was based on the observed HER performance, as discussed later. Overall, all sprayed NiAlMo coatings contained similar types of crystallites but with different phase distributions. The XRD image in

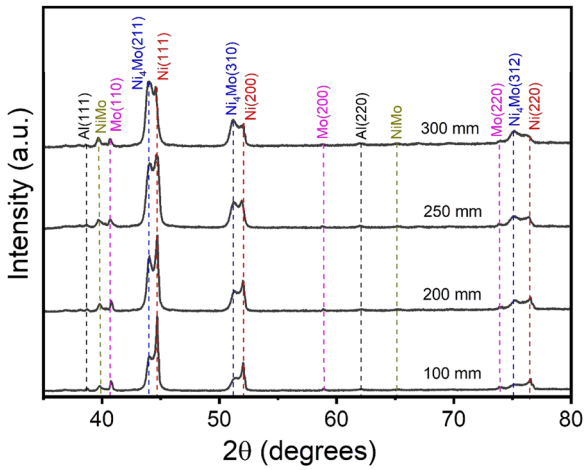

Fig. 2 XRD patterns of as-sprayed NiAlMo coatings using 20 kW of power and different spraying distances.

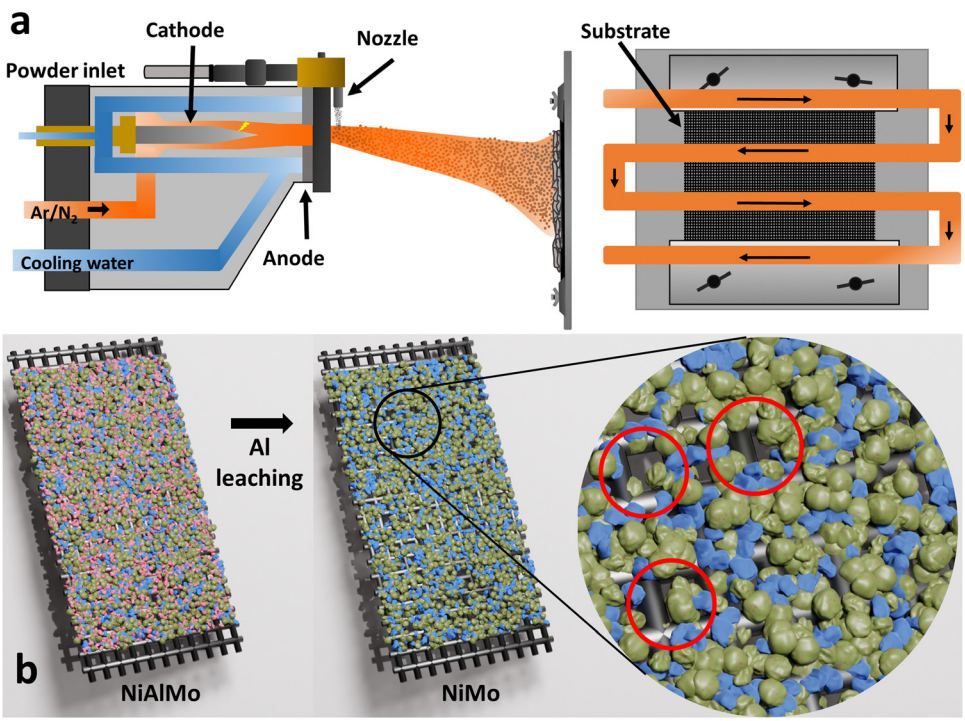

Fig. 1 (a) Schematic of the plasma torch spraying NiAlMo onto stainless-steel meshes using a raster spraying pattern (the arrows indicate the direction of the torch motion). (b) The as-sprayed coatings were later subjected to an Al leaching process to increase the porosity; the circles indicate the formed hollow structures due to Al removal. The green- and blue-coloured particles represent remaining Ni and Mo, respectively.

Open Access Article. Published on 07 July 2023. Downloaded on 1/22/2026 5:08:32 PM.
This article is licensed under a Creative Commons Attribution 3.0 Unported Licence.

Fig. 2 indicates the existence of pure Ni (AMCSD 0011153) with peaks at 44.53 (crystal plane (111)), 51.89 (200), and 76.45 (220). Al peaks are also seen at 38.50 (111), 44.76 (200), 65.16 (220), and 78.30 (311), while Mo (AMCSD 0011221) features are seen at 40.54 (110), 58.67 (200), and 73.74 (211). The coatings clearly contain a simple mixture of the three individual metals (Ni, Al, and Mo) present in the initial metallic powder (see Fig. S1, ESI†). However, there are some significant differences after the spraying process. The XRD features corresponding to Ni, Al, and Mo are significantly broader when compared to those seen in the powder precursor (Fig. S1, ESI†), indicating a much smaller crystalline size. Another difference is the formation of the tetragonal Ni_4Mo[12,25] with characteristics peaks at 31.27 (200), 43.58 (211), 50.44 (310), 51.4 (002), 74.12 (420), and 74.8 (312) as well as the equimolar NiMo alloy with peaks at 39.6 and 65.1, as reported by previous studies.[26–28] The as-sprayed samples are not subject to any annealing procedure, so the observed Ni–Mo alloys are formed in-flight after powder injection into the plasma and subsequently deposited on the substrate. This is further confirmed when producing samples with a spraying distance of 300 mm, where a significant contribution of alloyed Ni_4Mo and NiMo was still observable. At this distance, a maximum substrate temperature of 170 °C was reached, which is too low to significantly affect the already attached and solidified coating. On the other hand, using a shorter spraying distance of 100 mm resulted in a substrate temperature of nearly 300 °C. Under these conditions, the splats might grow and de-alloy, leading to larger Ni particles (as seen by sharper Ni peaks) and sharper features corresponding to Al and Mo. A similar trend was observed when increasing the power from 20 to 24 kW while maintaining the spraying distance constant at 250 mm, see Fig. S2 (ESI†), which results in a higher substrate temperature. Note that using shorter spraying distances (<100 mm) or a higher power causes (>38 kW) deformation and oxidation of both the stainless-steel substrate and coating occurred.

After the plasma spraying process, all coatings underwent an Al-leaching process for 24 h. The removal of Al is evidenced by XRD studies (reduced Al features in Fig. S3(a), ESI†) and EDX elemental mapping (Fig. 3). Due to the strong alkaline treatment, a partial oxidation of the surface is also expected, but the overall bulk samples are still metallic, as evidenced by XRD studies (Fig. S3(a), ESI†). Note that the removal of Al mostly occurs within the first 30 min of treatment, and only minor changes in morphology and catalytic activity were observed for longer Al leaching processes (Fig. 3, 4, and Fig. S3(b), ESI†). We noticed that the as-sprayed NiAlMo coating (20 kW@100 mm) exhibits a larger Al content than the powder precursor (Fig. 3(a and b)); this might be related to a preferential Al accumulation at the surface during the spraying process. The Al content is later reduced to 16.08 and 9.24 wt% after 0.5 h and 24 h of the leaching process. These results also indicate that the majority of Al is removed

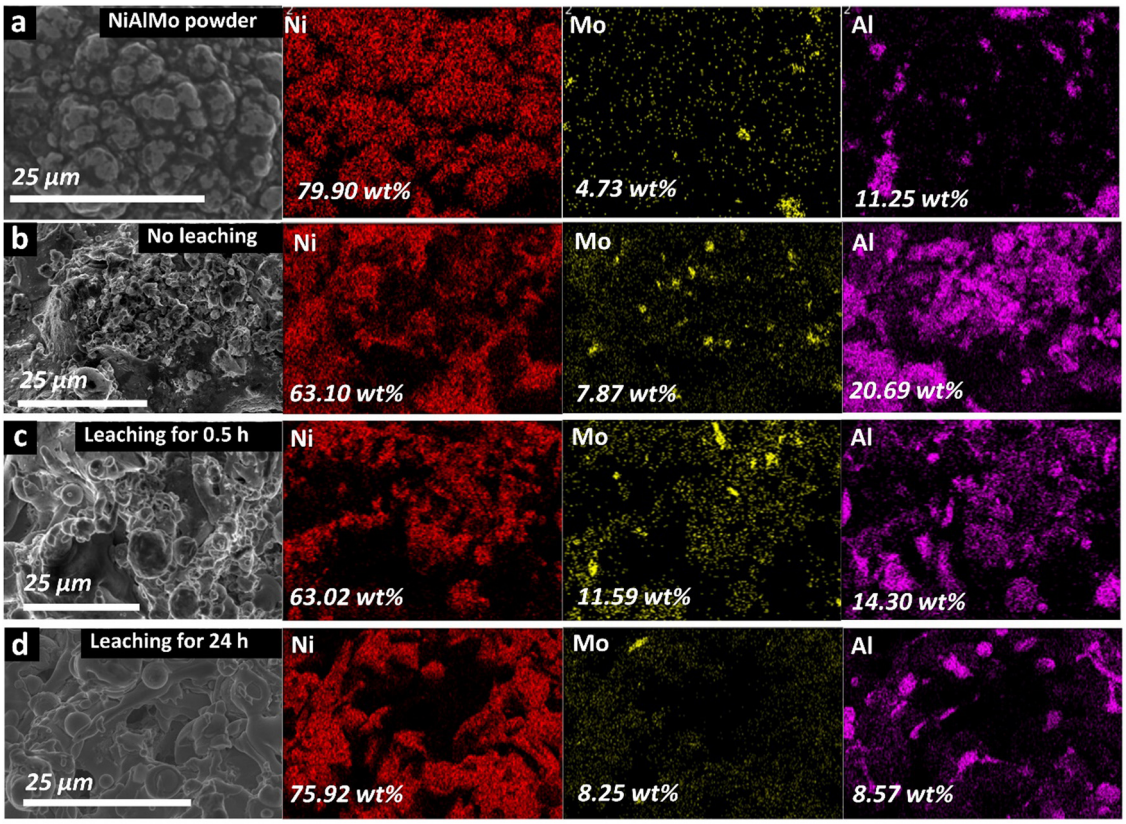

Fig. 3 SEM images and elemental EDX mapping of Ni, Mo, and Mo. (a) NiAlMo powder precursor. NiMo 20 kW@100 mm sample (b) before Al leaching, (c) after Al leaching for 0.5 h, and (d) after Al leaching for 24 h.

Open Access Article. Published on 07 July 2023. Downloaded on 1/22/2026 5:08:32 PM.
This article is licensed under a Creative Commons Attribution 3.0 Unported Licence.

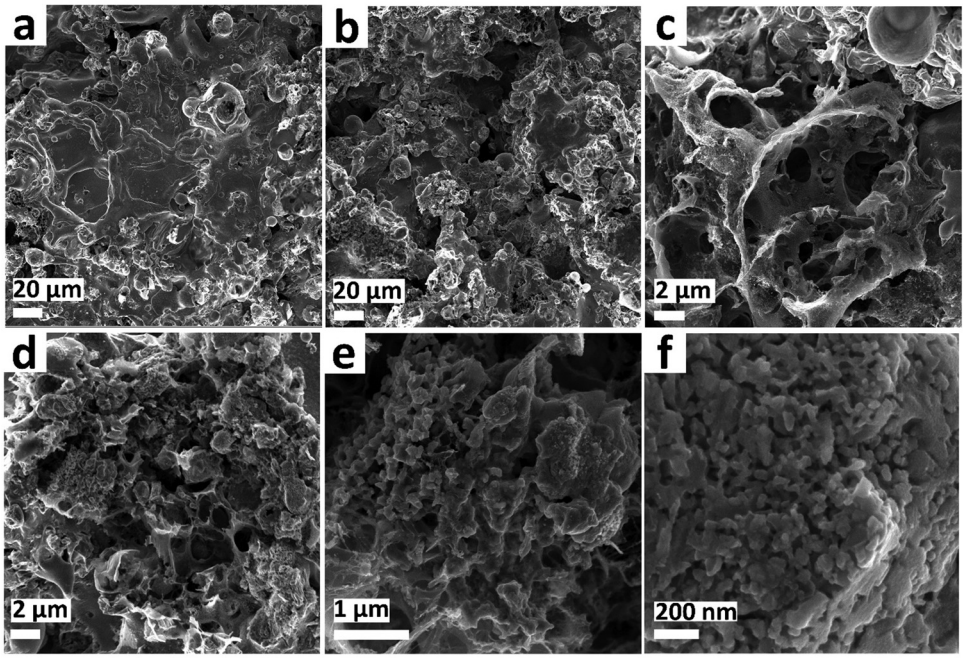

Fig. 4 SEM images of NiMo 20 kW@100 mm after Al leaching: (a and b) low magnification micrographs of the coating, and (c–f) higher magnification images showing the nanostructured features of the coating.

within the first 30 min. However, we kept the 24 h Al-leaching treatment to reduce the potential interference of Al removal during the catalytic tests. In addition, we evaluated changes in double-layer capacitance (C_{dl}) to identify the increase in surface area caused by the Al leaching step. Here, we used the optimal NiMo electrode for the HER, as discussed later, which was produced by using a power of 20 kW at a distance of 100 mm (labelled NiMo 20 kW@100 mm). To avoid side reactions, we use a non-aqueous electrolyte consisting of 0.1 M NBu_4PF_6 prepared in CH_3CN, Ag/Ag^+ (0.1 NBu_4PF_6, 0.01 M $AgNO_3$) as reference electrode (0.54 V *vs.* NHE), and a Pt wire as a counter electrode (see further details in the Experimental Section). The measurements were performed in triplicate. The voltammograms and evaluation of the C_{dl} of a representative sample are shown in Fig. S4 and S5 (ESI†), while a summary of all results is listed in Table S2 (ESI†). The as-sprayed sample exhibited a C_{dl} value of 3 mF cm^{-2}, while those exposed to a 24 h Al-leaching process achieved a C_{dl} of 14 mF cm^{-2}. This represents an increase of 366%, which directly correlates with a similar increase in surface area.

The surface morphology and microstructure of NiMo 20 kW@100 mm, the optimal electrode, were examined by scanning electron microscopy (SEM). As shown in Fig. 4(a, b) and Fig. S6 (ESI†), the sample presented an overall foam-like configuration with regions of dense solidified lava-like lamellar structures as well as porous structures under low magnification. Lamellar structures are formed when fully melted particles hit the substrate at a sufficient high velocity to spread over the substrate before solidification. These areas are dense and have a rather low surface roughness. On the other hand, particles that solidify before reaching the substrate form sliced and clustered structures as seen in Fig. 4(c–e). In addition, there are also defects as a result of unmelted particles and unsuccessful sputtering as well as gas pockets.[29] At higher magnification, it is possible to observe that the surface is composed of nanostructures and pores smaller than 200 nm seen in Fig. 4(f) and Fig. S6 (ESI†). As can be seen in Fig. S6 (ESI†), the surface structure before and after Al leaching exhibits similar features. The latter indicates that the sponge-like features and nanostructures had already formed before the Al-leaching processes.

The surface chemical state of the NiMo 20 kW@100 mm sample was investigated using X-ray photoelectron spectroscopy (XPS). The XPS survey spectrum (Fig. 5(a)) confirms the existence of Ni and Mo on the electrode surface. Fig. 5(b) shows the high-resolution XPS spectrum of Ni 2p; the main peaks are assigned to $Ni(OH)_2$ with two spin–orbit doublets at binding energies of 856.0 eV (Ni $2p_{3/2}$) and 873.6 eV (Ni $2p_{1/2}$). NiO (854.0/871.5 eV, $2p_{3/2}/2p_{1/2}$) and metallic Ni^{0+} (852.5/869.8 eV, $2p_{3/2}/2p_{1/2}$) are also observed. This information indicates that most of the surface is composed of oxidized Ni. Fig. 5(c) shows the Mo 3d spectrum in which deconvolution was performed by keeping a spin–orbital split distance of 3.15 eV and a 3 : 2 area ratio between $3d_{5/2}$ and $3d_{3/2}$.[30] Here, we detected the doublets associated with metallic Mo^{0+} (228.07 eV/231.22 eV, $3d_{5/2}$, $3d_{3/2}$) and partially oxidized Mo with three distinct oxidation states such as $Mo^{\delta+}$ ($0 < \delta < 4$: 229.09 eV/232.24 eV, $3d_{5/2}$, $3d_{3/2}$), Mo^{4+} (230.27 eV/233.42 eV, $3d_{5/2}$, $3d_{3/2}$), and Mo^{6+} (232.17 eV/235.32 eV, $3d_{5/2}$, $3d_{3/2}$).[31–33] The XPS spectrum of O 1s presented in Fig. 5(d) reveals the presence of metal hydroxides seen as a peak at 531.5 eV, in agreement with the Ni spectra. There are also two features at 529.9 eV and 533.3 eV attributed to lattice oxygen in metal oxides and adsorbed water at the

 This journal is © the Owner Societies 2023

Open Access Article. Published on 07 July 2023. Downloaded on 1/22/2026 5:08:32 PM.
This article is licensed under a Creative Commons Attribution 3.0 Unported Licence.

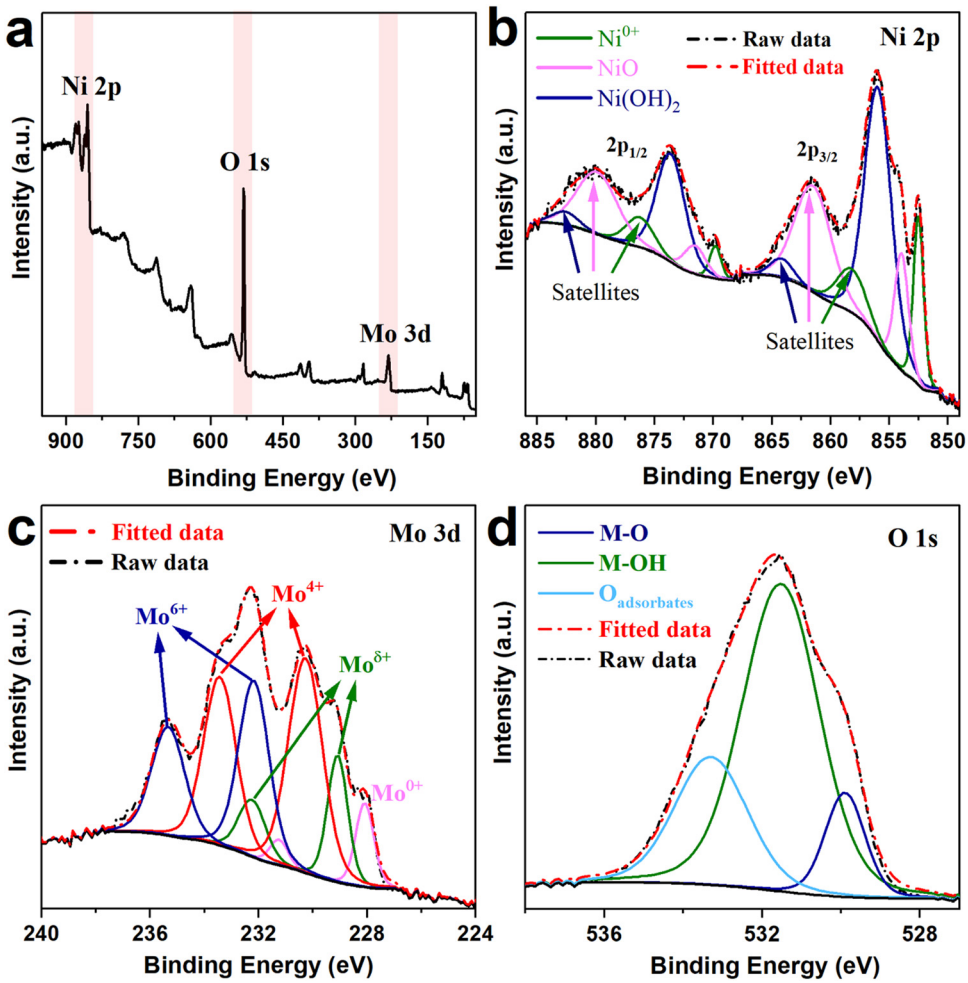

Fig. 5 (a) XPS survey spectrum; (b) core level spectra of Ni 2p, (c) Mo 3d, and (d) O 1s for the NiMo 20 kW@100 mm sample after Al leaching.

electrode surface, respectively. The presence of $Mo^{\delta+}$ and Mo^{4+}, as well as metallic Ni and Mo, suggests that the Al leaching produced a mild oxidation in a relatively thin surface layer.

Hydrogen evolution

The activity towards the hydrogen evolution reaction (HER) of the NiMo coatings was evaluated in the alkaline (1 M KOH) electrolyte. As previously mentioned, we first investigated the effect of the power used when creating the plasma while keeping the spraying distance at 250 mm. The results are summarized in Fig. 6(a). The observed trend in the overpotential (η_{10}) at -10 mA cm^{-2} (Tafel slope) was 19 (54 mV dec^{-1}), 65 (62 mV dec^{-1}), and 125 mV (106 mV dec^{-1}) for samples produced at 20, 24, and 38 kW, respectively. Uncoated stainless-steel meshes did not reach -10 mA cm^{-2} under the selected potential range (Fig. S7, ESI†). The best performance was obtained when using a power of 20 kW. The optimal spraying distance was later found by spraying electrodes at 100, 200, 250, and 300 mm away from the substrate while maintaining the power at 20 kW. The first major consequence of increasing the spraying distance from 100 to 300 mm is the decrease in catalyst loading from 200 to 78 mg cm^{-2} (see Table S3, ESI†), which also reduces the electrochemical active surface area from 1769 cm^2 per cm^2 of geometric area to 455 cm^2 per cm^2 (Table S3 and Fig. S8, ESI†). This resulted in different values for η_{50} (Tafel slope) of 42 mV (36 mV dec^{-1}), 46 mV (40 mV dec^{-1}), 62 mV (52 mV dec^{-1}), and 88 mV (74 mV dec^{-1}) for samples sprayed at 100, 200, 250, and 300 mm, respectively (Fig. 6(b and c)). The polarization curves in Fig. 6 have been corrected for *iR* drop, and the uncorrected curves can be seen in Fig. S9 (ESI†). For the best NiMo coating (20 kW@100 mm), the main HER process is a combined Volmer–Tafel mechanism.[4,34,35] The observed evolution of the Tafel slope from 36 to 74 mV dec^{-1} with reduced catalyst loading indicates a change from the Volmer–Tafel to Volmer–Heyrovsky route. The change in rate determining step suggests that samples with poor loading have less available active sites nearby for the Tafel step being relevant, and so, the Heyrovsky step dominates.[4,34,35] The observed HER activity exceeds previously reported values for complex hierarchical Ni_4Mo nanostructures described by the group of Luo, X,[12] where an overpotential of 108.5 mV to reach -50 mA cm^{-2} was reported. Meanwhile, our NiMo 20 kW@100 mm coating required solely 42 mV (*iR*-corrected), an excellent HER activity even when compared to the state-of-the-art Ni_4Mo produced by the group of Feng, X,[11] with an η_{10} of just 15 mV and a Tafel slope of 30 mV dec^{-1}. In addition, the NiMo

Open Access Article. Published on 07 July 2023. Downloaded on 1/22/2026 5:08:32 PM.
This article is licensed under a Creative Commons Attribution 3.0 Unported Licence.

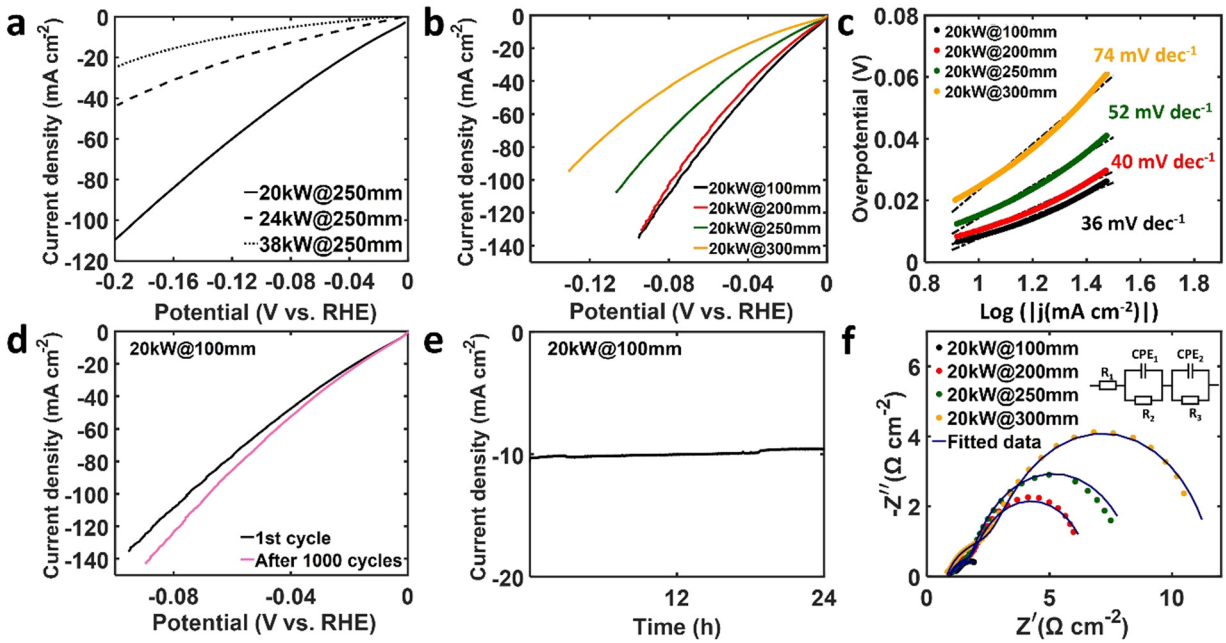

Fig. 6 (a) Polarization curves of samples sprayed at 250 mm but different spraying powers (without *iR* correction). (b) Polarization curves of samples sprayed at 20 kW but different distances (*iR*-corrected). (c) Tafel plots of samples in (b). (d) Polarization curve of NiMo 20 kW@100 mm before and after the 1000 CV cycles (*iR*-corrected). (e) Chronoamperometric response at constant potential to reach −10 mA cm^{-2} for 24 h. (f) Nyquist plot (0 *vs.* RHE); the inset represents the equivalent circuit.

20 kW@100 mm exhibits a good performance at high current densities requiring only 200 mV to reach 310 mA cm^{-2} (Fig. S10(a), ESI†), resulting in a mass activity of 0.65 A g^{-1} at this overpotential. This is an excellent value when compared to other noble-metal-free electrocatalysts,[36–38] see Table S4 (ESI†). The operational stability of NiMo 20 kW@100 mm was evaluated by a continuous CV cycling (1000 cycles), followed by a chronoamperometric test for 24 h. From Fig. 6(d), we observed that the activity was slightly increased by 10% as derived from the reduced η_{10}, attributed to improved wetting and removal of oxides produced during the Al leaching. The sample was subsequently subjected to a chronoamperometric test at a constant potential required to reach −10 mA cm^{-2} for 24 hours with negligible signs of degradation (Fig. 6(e)), in line with previous Ni_4Mo studies.[9,11,12] Electrochemical impedance spectroscopy (EIS) was used to evaluate the Nyquist plots (Fig. 6(f)). These exhibit two semicircles that can be modelled using the equivalent circuit diagram shown in the inset of Fig. 6(f) comprising two parallel CPE-R (CPE: constant phase element) components connected in series. The semicircle in the high-frequency range is commonly observed in highly porous electrodes,[39–41] and it has been associated with a variety of processes such as pseudocapacitive charge storage (*e.g.*, ion intercalation)[41] or electrolyte resistance inside the porous electrodes.[42] The second semicircle in the low-frequency range corresponds to the reaction kinetics for the HER.[42,43] The bulk electrolyte resistance is represented by the element R_1. In Fig. 6(f), both semicircles decrease, and so the value of the resistor R_3, at smaller spraying distances. R_3 is associated with the charge-transfer resistances with a value of 1.07, 4.67, 6.65 and 8.73 Ω cm^{-2} for NiMo electrodes sprayed at 100, 200, 250, and 300 mm away, respectively, in agreement with the electrochemical response and Tafel slopes.

Theoretical simulations were carried out to evaluate the hydrogen adsorption energy on the predominant Ni_4Mo phase. We prepared four crystal surfaces ((101), (110), (121), and (211)) that have been previously reported to be active towards HER.[12,44,45] We then evaluated the hydrogen adsorption free energy (ΔG_H), a measure of the hydrogen–surface interaction strength, to estimate its catalytic activity. The usage of ΔG_H as a descriptor towards the HER activity can be understood *via* the Sabatier principle, which states that optimal binding energies should be neither too strong nor too weak.[4,19] In other words, electrocatalysts with strong hydrogen–surface interactions will experience an inhibited HER activity due to slow hydrogen recombination (*e.g.*, Heyrovsky or Tafel step). On the other hand, weak hydrogen–surface interactions will result in a slow proton transfer (*e.g.*, Volmer step) since hydrogen adsorption is no longer favourable. As a result of this interplay, the optimal value of ΔG_H for the HER is zero. This relationship gives rise to a Volcano-like plot of the logarithm of the exchange current density (j_0) with ΔG_H, where the top of the Volcano lies at the optimal value of $\Delta G_H = 0$, as seen in Fig. 7(a). For the sake of clarity, we delimited a green region ($-0.07 < \Delta G_H < 0.07$ eV) that we consider to be optimum, and it is in this region where the highly active Pt(111) surface can be found, while the bare Ni(111) surface lies towards the left side with values of $\Delta G_H < 0$ (strong H-interaction).[4] As seen from the Volcano plot, the selected Ni_4Mo surfaces exhibit a large variety of adsorption sites due to their unique surface termination. These are mostly Ni atoms with different local atomic coordinations (see Fig. S11

Open Access Article. Published on 07 July 2023. Downloaded on 1/22/2026 5:08:32 PM.
This article is licensed under a Creative Commons Attribution 3.0 Unported Licence.

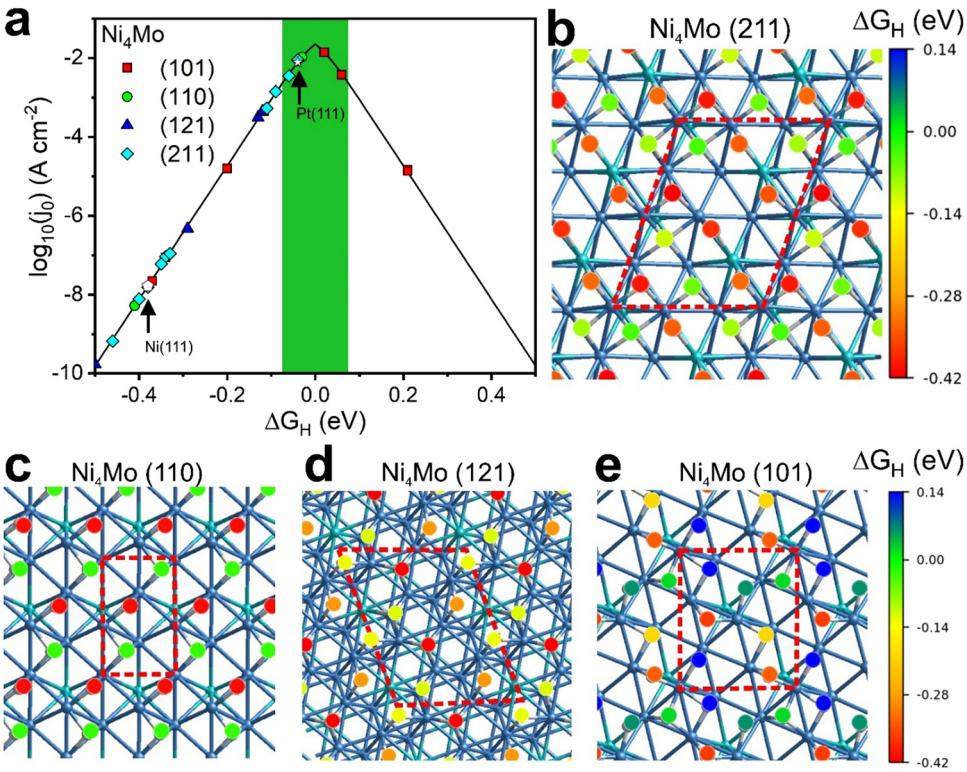

Fig. 7 (a) HER volcano plot of various Ni_4Mo surfaces. The solid line represents the microkinetic model developed by Nørskov and collaborators.[19] The optimum adsorption free energy of hydrogen was defined as $-0.07 < \Delta G_H < 0.07$ eV, highlighted by the green area. The pentagon and star indicate the activity of Ni(111) and Pt(111). (b–e) HER activity maps for various Ni_4Mo surfaces. The optimum ΔG_H is also highlighted in green. Positive (negative) values of ΔG_H indicate weak (strong) hydrogen adsorption seen in blue (red). The red dashed line indicates the unit cell used during the study. Only the top two atomic layers are shown for clarity. Colour code: blue (cyan) represents Ni (Mo).

(ESI†)), which leads to a large variety of hydrogen adsorption energies spanning from −0.5 up to +0.2 eV. The latter results in a clear heterogeneity in the HER activity that is often seen in defective systems.[46,47] Interestingly, there are several sites, in particular in the (211) and (101) Ni_4Mo surfaces, that exhibit ΔG_H in the optimal range similar to Pt (111). This can be understood by considering that in the tetragonal Ni_4Mo, the twelve nearest neighbours of Mo are Ni, while for Ni, three out of the nearest neighbours are Mo. In this configuration, the Ni–Ni and Ni–Mo bond lengths are nearly identical (2.55 Å)[25] but have larger values than the Ni–Ni distance in pure nickel (2.49 Å). This stronger interaction leads to unique band structures with partially empty d-orbitals similar to Pt,[9] effectively tuning the hydrogen adsorption energy.

Fig. 7(b–e) depict the activity maps indicating the spatial distribution of the catalytic sites. The optimum adsorption energy is indicated in green. We noticed that the most active sites (those with ΔG_H near the optimum) are the fcc sites near Mo atoms, where only Ni atoms constitute the fcc site. In other words, Mo was not part of the adsorption site, but its nearby influence directly tuned the hydrogen–surface interaction and so the HER activity. These results suggest that the excellent HER activity seen in Ni_4Mo is originated from the multiple sites in diverse crystal structures that exhibit near optimal hydrogen–surface interaction. In addition to hydrogen adsorption, water dissociation plays a key role in the multi-step alkaline HER since it is the source of adsorbed H. Therefore, we evaluated the dissociation energy (E_{diss}) of water into adsorbed H* and HO* intermediates as an indicator of how feasible the sluggish water dissociation step can be accomplished. We found that the E_{diss} on Ni_4Mo surfaces (see Fig. S12 and S13, ESI†) is generally larger than that on pure Ni. For example, Ni(101) and Ni(111) surfaces exhibit an E_{diss} of −0.89 and −0.40 eV, respectively, while the (101), (110), and (121) Ni_4Mo surfaces showed an E_{diss} of −0.51, −0.96, and −1.16 eV, respectively. Note that negative values of E_{diss} indicate a favourable configuration. The stronger interaction of H* and HO* intermediates on Ni_4Mo can result in a reduced energy barrier of the Volmer step, effectively improving the overall HER activity.[48–50]

Oxygen evolution

We carried out a similar optimization scheme for the oxygen evolution reaction (OER) where the best electrocatalyst was the NiMo coating sprayed at 100 mm with 16 kW of power (Fig. S14, ESI†). This coating exhibits a similar phase composition and morphology to the samples produced for the HER, with XRD studies (Fig. S15, ESI†) showing the presence of the three individual metals (Ni, Al, Mo) and the alloyed (Ni_4Mo, NiMo) phases. Due to the lower power, NiMo 16 kW@100 mm has a lower catalyst loading of just 147 mg cm^{-2}. SEM images

Open Access Article. Published on 07 July 2023. Downloaded on 1/22/2026 5:08:32 PM.
This article is licensed under a Creative Commons Attribution 3.0 Unported Licence.

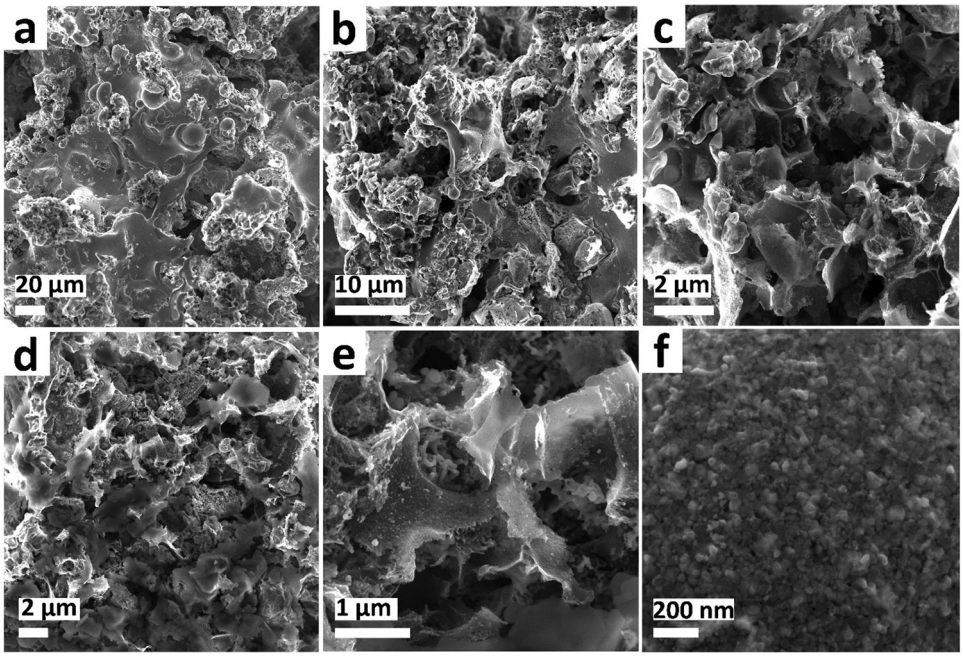

Fig. 8 SEM images of NiMo 16 kW@100 mm coating after Al leaching: (a and b) low magnification micrographs of the coating, and (c–f) higher magnification images showing the nanostructured features of the coating.

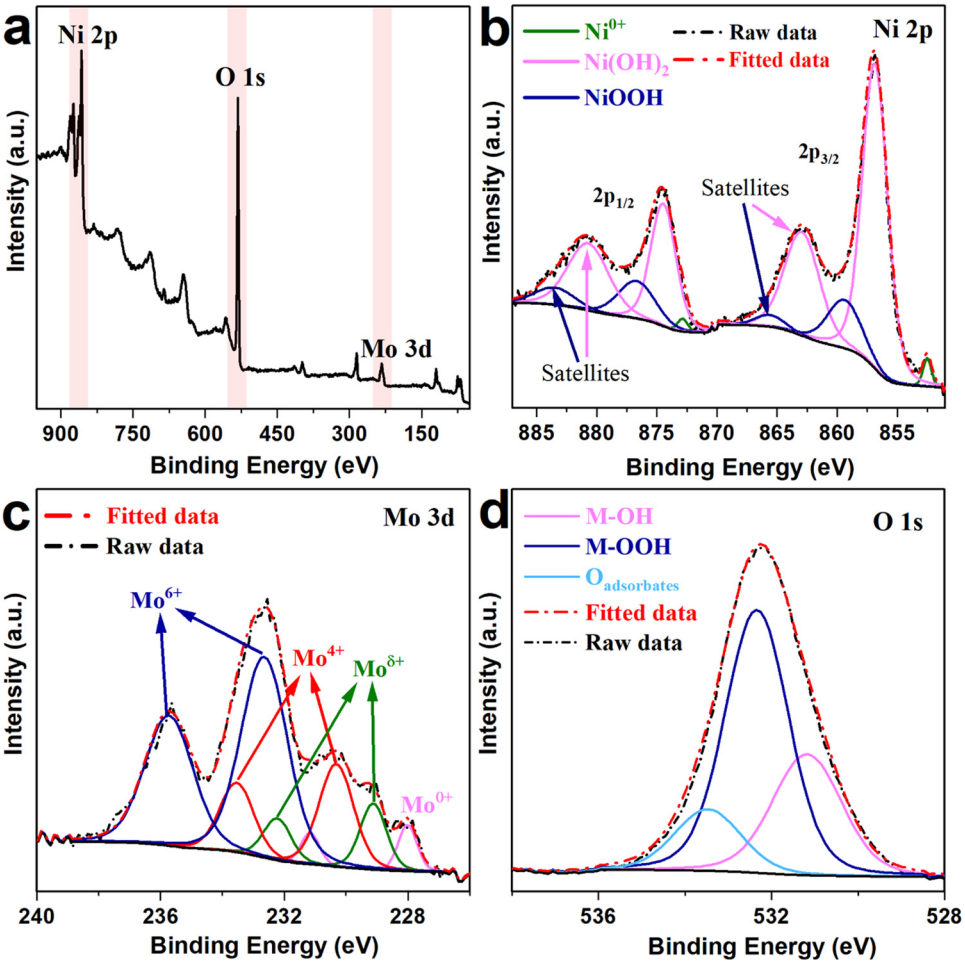

Fig. 9 (a) XPS survey spectrum; (b) spectra of Ni 2p, (c) Mo 3d, and (d) O 1s of the NiMo 16 kW@100 mm sample after Al leaching.

 This journal is © the Owner Societies 2023

Open Access Article. Published on 07 July 2023. Downloaded on 1/22/2026 5:08:32 PM.
This article is licensed under a Creative Commons Attribution 3.0 Unported Licence.

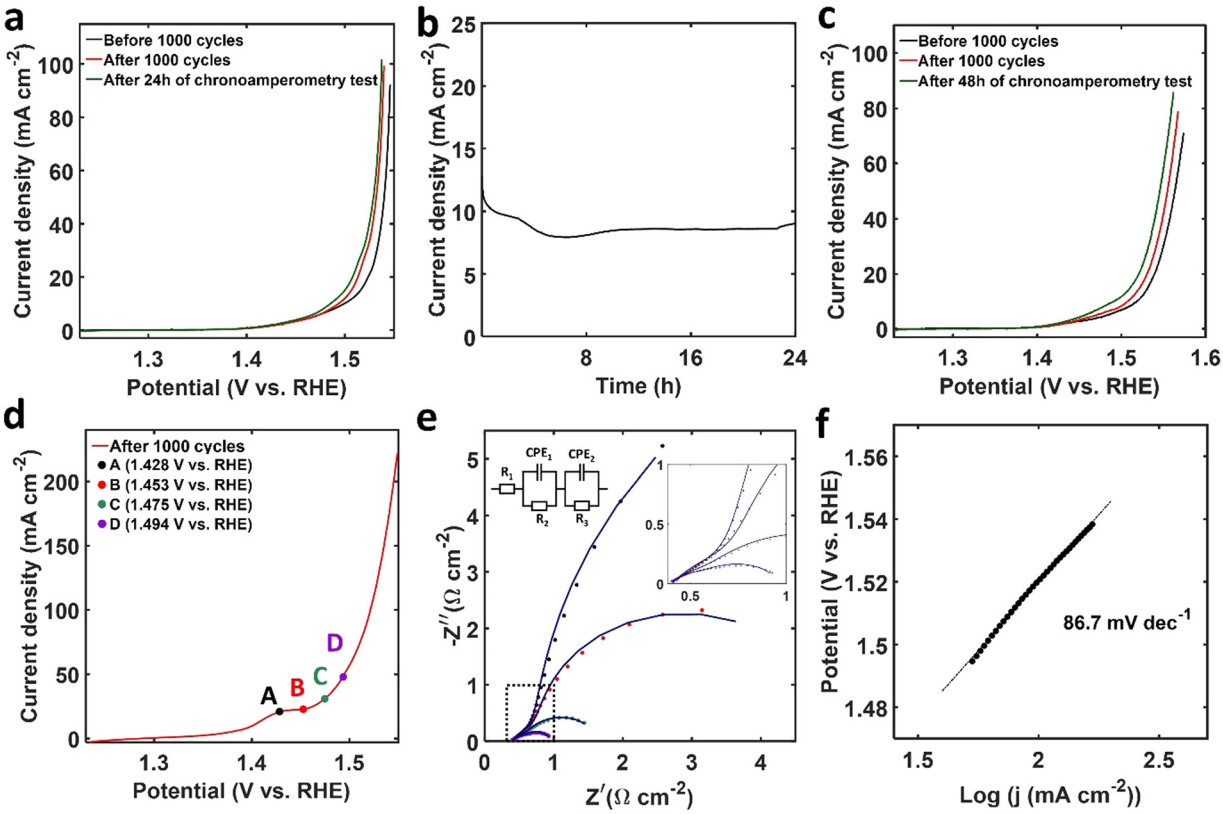

Fig. 10 (a) *iR*-corrected polarization curves of NiMo 16 kW@100 mm before 1000 cycles of CV activation, after activation and after 24 h of chronopotentiometry test. (b) Chronoamperometric response at a constant potential to reach 10 mA cm^{-2} for 24 h. (c) *iR*-corrected polarization curves of NiMo 16 kW@100 mm before activation (black line), after activation (red line), and after 48 h at a constant potential to reach 50 mA cm^{-2}. (d) *iR*-corrected polarization curves of 2 month-aged NiMo 16 kW@100 mm after activation (1000 CVs). (e) Nyquist plots at different potentials indicated in (d); the equivalent circuit model is shown, and the inset represents a closeup at high frequencies. (f) Tafel plot of (d) evaluated from 50 to 150 mA cm^{-2}.

(Fig. 8(a–f) and Fig. S16, ESI†) revealed that the coating exhibits a lamellar structure (Fig. S16(d), ESI†), where at higher magnification, a porous structure with thin flakes (Fig. 8(b–e) and Fig. S16(e), ESI†) is observed. A closeup to the surfaces also reveals the presence of nanosized bumps and particles well under 200 nm (Fig. 8(f) and Fig. S16(f), ESI†). A major difference with coatings fabricated at a higher power is the apparent larger porosity with a foam-like structure formed by interconnected bridges surrounded by large voids. Note that the porous structure is formed during the spraying process and not after Al leaching as seen in Fig. S16 (ESI†).

Fig. 9(a) shows the XPS survey spectrum for the NiMo 16 kW@100 mm sample. We noticed a substantial higher oxidized surface when compared to NiMo 20 kW@100 mm coating due to the appearance of NiOOH and less Ni metallic. We also found a larger Mo oxide to Mo metal ratio (22.3 for NiMo 16 kW@100 mm and 20.1 for NiMo 20 kW@100 mm). The high-resolution Ni 2p spectrum (Fig. 9(b)) is now dominated by $Ni(OH)_2$ (856.9 eV/874.5 eV, $2p_{3/2}/2p_{1/2}$) and NiOOH (859.4 eV/876.6 eV, $2p_{3/2}/2p_{1/2}$),[51–53] with a slight contribution from metallic Ni^{0+} (852.5 eV/872.8 eV, $2p_{3/2}/2p_{1/2}$). Similarly, the Mo 3d spectrum (Fig. 9(c)) shows a larger contribution of high-valence Mo, such as Mo^{6+} (232.66 eV/235.81 eV, $3d_{5/2}$, $3d_{3/2}$) and Mo^{4+} (230.3 eV/233.45 eV, $3d_{5/2}$, $3d_{3/2}$), while metallic Mo^{0+} (228.0 eV/231.15 eV) and $Mo^{\delta+}$ (229.12 eV/232.27 eV) are present in a lower extent.[54] The XPS spectrum of O 1s in Fig. 9(d) agrees well with the increased hydroxides (531.2 eV) and oxo-hydroxides (532.3 eV) seen in the Ni and Mo spectra.[51,53]

Before evaluating the OER activity, the electrode was first activated by cyclic voltammetry (1000 cycles) under anodic conditions (1.0 to 1.6 V *vs.* RHE, 50 mV s^{-1}). The reported activity was recorded by performing a final CV scan with a scan rate of 1 mV s^{-1} in a potential range of 1.23 to 1.63 V *vs.* RHE. Note that the contribution of the stainless-steel mesh (Fig. S17, ESI†) is minimal under the studied potential range. As can be seen in Fig. 10(a), the performance of the electrocatalyst was enhanced after 1000 CVs, evidenced by the reduction of η_{50} from 310 to 303 mV. The observed activity is in line with other previously mentioned Ni_4Mo nanostructures reported by Luo, X,[12] where an overpotential of ~290 mV was required to achieve 50 mA cm^{-2}. In addition, the NiMo 16 kW@100 mm sample exhibited a good performance at high current densities (Fig. S10(b), ESI†) as well as a competitive mass activity of 0.3 A g^{-1} at an overpotential of 300 mV, in agreement with other noble-metal-free electrocatalysts,[55–57] see also Table S5 (ESI†) for further comparison. The stability test was initially conducted by applying a constant potential large enough to achieve a current density of 10 mA cm^{-2} for 24 h, and the chronoamperometric (CA) response is plotted in Fig. 10(b).

Open Access Article. Published on 07 July 2023. Downloaded on 1/22/2026 5:08:32 PM.
This article is licensed under a Creative Commons Attribution 3.0 Unported Licence.

The initial variation of the current density can be related to the transpassivation of Ni. After the stability test, an additional polarization curve was recorded under the same potential region, and only a slight increment in catalyst activity was observed (black line in Fig. 10(a)). To further evaluate the stability of NiMo 16 kW@100 mm, a new sample was subjected to a larger anodic potential to reach 50 mA cm^{-2} for 48 h continuously. The change in OER activity was evaluated by recording three polarization curves at different stages in the process: (i) before activation, (ii) after activation, and (iii) after 48 h stability test. The results are shown in Fig. 10(c), and we can see that for this sample, the η_{50} decreases from 330 to 326 mV after the activation process, and a further reduction is observed after 48 h CA test to 315 mV. These results confirm the great operational stability of the NiMo electrocatalysts.

In addition, we evaluated the OER activity of an aged NiMo 15.6 kW@100 mm sample that was subjected to the Al-leaching process and then stored in DI water for 2 months. We carried out the exact same activation procedure as other samples before evaluating its OER activity. The *iR*-corrected polarization curve after activation is shown in Fig. 10d. A clear oxidation feature related to Ni^{2+}/Ni^{3+} at ~1.43 V *vs.* RHE is observed. This feature is not seen in fresh samples under similar measurement conditions, suggesting the formation of nickel hydroxides during the sample storage. The latter can also explain the enhanced OER activity observed (η_{50} = 256 mV) when compared to fresh samples (η_{50} = 303 mV). We performed EIS measurements at different potentials (1.428 V, 1.453 V, 1.475 V, and 1.494 V *vs.* RHE), indicated in Fig. 10d, to investigate the activation of the OER. The corresponding Nyquist plots are shown in Fig. 10e. Similar to the results in Fig. 6f, the Nyquist plots exhibit two semicircles that can be modelled by an equivalent circuit containing two parallel CPE-R components in series (see the inset in Fig. 10e). We observe that R_1 (0.42 Ω at 1.428 V *vs.* RHE) and R_2 (0.36 Ω at 1.428 V *vs.* RHE) are similar irrespective of the applied potential (see Table S6, ESI†). The latter is expected for the Ohmic resistance (R_1), while R_2 must be associated with a process such as charge storage. For the case of R_3, there is a clear reduction from 17.59 to 0.20 Ω when increasing the potential, as expected for a faradaic process in which there is a decrease in the energy barriers for the electron-transfer reactions with the overpotential, such as the OER. Finally, we evaluated the Tafel slope (Fig. 10f) in the current range of 50 to 150 mA cm^{-2}, resulting in a value of 86.7 mV dec^{-1}; this is comparable to other highly active Ni-based electrocatalysts such as NiOOH.[58]

Conclusions

Nanostructured Ni–Mo coatings were deposited directly onto stainless-steel meshes *via* atmospheric plasma spraying. The material mainly consisted of Ni and Ni_4Mo having a highly porous configuration with a foam-like structure. The material loading was easily varied from 78 up to 200 mg cm^{-2} without affecting the morphology. The produced Ni–Mo coatings were active towards both HER and OER in the alkaline electrolyte. An exceptional HER activity was seen for samples produced at 20 kW and 100 mm of spraying distance where an η_{50} of just 42 mV and a Tafel slope of 36 mV dec^{-1} were observed, with a mass activity of 0.65 A g^{-1} at an overpotential of 200 mV. Theoretical simulations indicated that the excellent HER activity was a consequence of near optimal hydrogen–surface interactions and improved water dissociation seen in several crystalline Ni_4Mo surfaces. For the oxygen evolving electrode, a lower catalyst loading of 147 mg cm^{-2} was beneficial because of the formation of a thinner catalyst layer, which improved the formation of NiOOH. The optimized electrode exhibited an η_{50} of 310 mV and a mass activity of 0.3 A g^{-1} at an overpotential of 300 mV, and no deterioration was observed even after 48 h of operation at a constant potential. These results show the potential of using APS systems as a scalable production technique to form the highly active Ni_4Mo alloy.

Conflicts of interest

There are no conflicts to declare.

Acknowledgements

The authors acknowledge support from Vetenskapsrådet (2018-03937), the Kempe Foundation (JCK-2132), the Carl Tryggers Foundation (CTS 21-1581), and the Swedish Foundation for Strategic Research (SSF-Agenda 2030 – PUSH). The computations were enabled by resources provided by the National Academic Infrastructure for Supercomputing in Sweden (NAISS) and the Swedish National Infrastructure for Computing (SNIC) at the National Supercomputer Centre (NSC) in Linköping University and the PDC Center for High Performance Computing in KTH Royal Institute of Technology partially funded by the Swedish Research Council through grant agreement no. 2022-06725 and no. 2018-05973. We also thank the Umeå Core Facility for Electron Microscopy (UCEM), the Vibrational Spectroscopy Core Facility (ViSp), and the XPS platform at Umeå University.

References

1 L. Huo, C. Jin, K. Jiang, Q. Bao, Z. Hu and J. Chu, Applications of Nickel-Based Electrocatalysts for Hydrogen Evolution Reaction, *Adv. Energy Sustainability Res.*, 2022, **3**(4), 2100189, DOI: **10.1002/aesr.202100189**.
2 M. Ďurovič, J. Hnát and K. Bouzek, Electrocatalysts for the hydrogen evolution reaction in alkaline and neutral media. A comparative review, *J. Power Sources*, 2021, **493**, 229708, DOI: **10.1016/j.jpowsour.2021.229708**.
3 M. Carmo and D. Stolten, Energy Storage Using Hydrogen Produced From Excess Renewable Electricity: Power to Hydrogen, in *Science and Engineering of Hydrogen-Based Energy Technologies*, ed. P. E. V. de Miranda, Academic Press, 2019, ch. 4, p. 165.

Open Access Article. Published on 07 July 2023. Downloaded on 1/22/2026 5:08:32 PM.
This article is licensed under a Creative Commons Attribution 3.0 Unported Licence.

4 J. Ekspong, E. Gracia-Espino and T. Wågberg, Hydrogen Evolution Reaction Activity of Heterogeneous Materials: A Theoretical Model, *J. Phys. Chem. C*, 2020, **124**(38), 20911, DOI: 10.1021/acs.jpcc.0c05243.
5 C. Zou, X. Guo, F. Wang, R. Tian, Y. Hou, F. Liu and H. Yang, Macroporous Ni-Fe hydroxide bifunctional catalyst for efficient alkaline water splitting, *J. Sol-Gel Sci. Technol.*, 2022, **103**, 505–514, DOI: 10.1007/s10971-022-05793-1.
6 B. Buccheri, F. Ganci, B. Patella, G. Aiello, P. Mandin and R. Inguanta, Ni–Fe alloy nanostructured electrodes for water splitting in alkaline electrolyser, *Electrochim. Acta*, 2021, **388**, 138588, DOI: 10.1016/j.electacta.2021.138588.
7 F.-H. Yuan, M.-R. Mohammadi, L.-L. Ma, Z.-D. Cui, S.-L. Zhu, Z.-Y. Li, S.-L. Wu, H. Jiang and Y.-Q. Liang, Electrodeposition of self-supported NiMo amorphous coating as an efficient and stable catalyst for hydrogen evolution reaction, *Rare Met.*, 2022, **41**, 2624–2632, DOI: 10.1007/s12598-022-01967-6.
8 H. Chen, S. Qiao, J. Yang and X. Du, NiMo/$NiCo_2O_4$ as synergy catalyst supported on nickel foam for efficient overall water splitting, *Mol. Catal.*, 2022, **518**, 112086, DOI: 10.1016/j.mcat.2021.112086.
9 Y. Zhou, M. Luo, W. Zhang, Z. Zhang, X. Meng, X. Shen, H. Liu, M. Zhou and X. Zeng, Topological Formation of a Mo–Ni-Based Hollow Structure as a Highly Efficient Electrocatalyst for the Hydrogen Evolution Reaction in Alkaline Solutions, *ACS Appl. Mater. Interfaces*, 2019, **11**(24), 21998, DOI: 10.1021/acsami.9b03686.
10 M. Rafei, X. Wu, A. Piñeiro Garcia, V. Miranda la Hera, T. Wågberg and E. Gracia-Espino, Non-Stoichiometric NiFeMo Solid Solutions; Tuning the Hydrogen Adsorption Energy *via* Molybdenum Incorporation, *Adv. Mater. Interfaces*, 2022, **9**(34), 2201214, DOI: 10.1002/admi.202201214.
11 J. Zhang, T. Wang, P. Liu, Z. Liao, S. Liu, X. Zhuang, M. Chen, E. Zschech and X. Feng, Efficient hydrogen production on MoNi4 electrocatalysts with fast water dissociation kinetics, *Nat. Commun.*, 2017, **8**(1), 15437, DOI: 10.1038/ncomms15437.
12 J. Xiao, D. Cai, Y. Zhang and X. Luo, Ni_4Mo alloy nanosheets coating on carbon tube arrays as high-performance electrocatalyst toward overall water splitting, *J. Alloys Compd.*, 2021, **886**, 161180, DOI: 10.1016/j.jallcom.2021.161180.
13 H. Ding, L. Xu, C. Wen, J.-J. Zhou, K. Li, P. Zhang, L. Wang, W. Wang, W. Wang and X. Xu, Surface and interface engineering of MoNi alloy nanograins bound to Mo-doped NiO nanosheets on 3D graphene foam for high-efficiency water splitting catalysis, *Chem. Eng. J.*, 2022, **440**, 135847, DOI: 10.1016/j.cej.2022.135847.
14 P. Kuang, T. Tong, K. Fan and J. Yu, In Situ Fabrication of Ni–Mo Bimetal Sulfide Hybrid as an Efficient Electrocatalyst for Hydrogen Evolution over a Wide pH Range, *ACS Catal.*, 2017, **7**(9), 6179, DOI: 10.1021/acscatal.7b02225.
15 E. Cossar, M. S. E. Houache, Z. Zhang and E. A. Baranova, Comparison of electrochemical active surface area methods for various nickel nanostructures, *J. Electroanal. Chem.*, 2020, **870**, 114246, DOI: 10.1016/j.jelechem.2020.114246.
16 T. Shinagawa, A. T. Garcia-Esparza and K. Takanabe, Insight on Tafel slopes from a microkinetic analysis of aqueous electrocatalysis for energy conversion, *Sci. Rep.*, 2015, **5**(1), 13801, DOI: 10.1038/srep13801.
17 R. A. Scott and C. M. Lukehart, *Applications of Physical Methods to Inorganic and Bioinorganic Chemistry*, Wiley, 2007.
18 N. Manfredi, C. Decavoli, C. L. Boldrini, C. Coluccini and A. Abbotto, Ferrocene Derivatives Functionalized with Donor/Acceptor (Hetero)Aromatic Substituents: Tuning of Redox Properties, *Energies*, 2020, **13**(15), 3937, DOI: 10.3390/en13153937.
19 J. K. Nørskov, T. Bligaard, A. Logadottir, J. R. Kitchin, J. G. Chen, S. Pandelov and U. Stimming, Trends in the Exchange Current for Hydrogen Evolution, *J. Electrochem. Soc.*, 2005, **152**(3), J23, DOI: 10.1149/1.1856988.
20 J. Ekspong and E. Gracia-Espino, Theoretical Analysis of Surface Active Sites in Defective 2H and 1T′ MoS_2 Polymorphs for Hydrogen Evolution Reaction: Quantifying the Total Activity of Point Defects, *Adv. Theory Simul.*, 2020, **3**(3), 1900213, DOI: 10.1002/adts.201900213.
21 J. M. Soler, E. Artacho, J. D. Gale, A. García, J. Junquera, P. Ordejón and D. Sánchez-Portal, The SIESTA method forab initioorder-Nmaterials simulation, *J. Phys.: Condens. Matter*, 2002, **14**(11), 2745, DOI: 10.1088/0953-8984/14/11/302.
22 F. Razmjooei, T. Liu, D. A. Azevedo, E. Hadjixenophontos, R. Reissner, G. Schiller, S. A. Ansar and K. A. Friedrich, Improving plasma sprayed Raney-type nickel-molybdenum electrodes towards high-performance hydrogen evolution in alkaline medium, *Sci. Rep.*, 2020, **10**(1), 10948, DOI: 10.1038/s41598-020-67954-y.
23 F. Razmjooei, A. Farooqui, R. Reissner, A. S. Gago, S. A. Ansar and K. A. Friedrich, Elucidating the Performance Limitations of Alkaline Electrolyte Membrane Electrolysis: Dominance of Anion Concentration in Membrane Electrode Assembly, *ChemElectroChem*, 2020, **7**(19), 3951, DOI: 10.1002/celc.202000605.
24 F. Razmjooei, R. Reißner, A. S. Gago and A. Ansar, Highly Active Binder Free Plasma Sprayed Non-Noble Metal Electrodes for Anion Exchange Membrane Electrolysis at Different Reduced KOH Concentrations, *ECS Trans.*, 2019, **92**(8), 689, DOI: 10.1149/09208.0689ecst.
25 D. Harker, The Crystal Structure of Ni_4Mo, *J. Chem. Phys.*, 1944, **12**(7), 315, DOI: 10.1063/1.1723945.
26 K. Hashimoto, T. Sasaki, S. Meguro and K. Asami, Nanocrystalline electrodeposited Ni–Mo–C cathodes for hydrogen production, *Mater. Sci. Eng., A*, 2004, **375–377**, 942, DOI: 10.1016/j.msea.2003.10.300.
27 J. M. Jakšić, M. V. Vojnović and N. V. Krstajić, Kinetic analysis of hydrogen evolution at Ni–Mo alloy electrodes, *Electrochim. Acta*, 2000, **45**(25), 4151, DOI: 10.1016/S0013-4686(00)00549-1.
28 L. S. Sanches, S. H. Domingues, C. E. B. Marino and L. H. Mascaro, Characterisation of electrochemically deposited Ni–Mo alloy coatings, *Electrochem. Commun.*, 2004, **6**(6), 543, DOI: 10.1016/j.elecom.2004.04.002.
29 F. Ghadami, M. Heydarzadeh Sohi and S. Ghadami, Effect of TIG surface melting on structure and wear properties of air plasma-sprayed WC–Co coatings, *Surf. Coat. Technol.*, 2015, **261**, 108, DOI: 10.1016/j.surfcoat.2014.11.050.

Open Access Article. Published on 07 July 2023. Downloaded on 1/22/2026 5:08:32 PM.
This article is licensed under a Creative Commons Attribution 3.0 Unported Licence.

30 M. Lv, W. Xie, S. Sun, G. Wu, L. Zheng, S. Chu, C. Gao and J. Bao, Activated-carbon-supported K–Co–Mo catalysts for synthesis of higher alcohols from syngas, *Catal. Sci. Technol.*, 2015, **5**(5), 2925, DOI: 10.1039/c5cy00083a.

31 J. Gong, Y. Kong, J. Li, X. Wang, Y. Que, Z. Zhang, Z. Ding and X. Xiao, Role of surface microstructure of Mo back contact on alkali atom diffusion and Ga grading in Cu(In,Ga)Se_2 thin film solar cells, *Energy Sci. Eng.*, 2019, **7**(3), 754, DOI: 10.1002/ese3.304.

32 G. Seifert, J. Finster and H. Müller, SW Xα calculations and X-ray photoelectron spectra of molybdenum(II) chloride cluster compounds, *Chem. Phys. Lett.*, 1980, **75**(2), 373, DOI: 10.1016/0009-2614(80)80534-3.

33 C. L. Bianchi, M. G. Cattania and P. Villa, XPS characterization of Ni and Mo oxides before and after "in situ" treatments, *Appl. Surf. Sci.*, 1993, **70**, 211.

34 R. Parsons, The rate of electrolytic hydrogen evolution and the heat of adsorption of hydrogen, *Trans. Faraday Soc.*, 1958, **54**, 1053, DOI: 10.1039/TF9585401053.

35 T. Shinagawa, A. T. Garcia-Esparza and K. Takanabe, Insight on Tafel slopes from a microkinetic analysis of aqueous electrocatalysis for energy conversion, *Sci. Rep.*, 2015, **5**(1), 1.

36 Z. Zhuang, S. A. Giles, J. Zheng, G. R. Jenness, S. Caratzoulas, D. G. Vlachos and Y. Yan, Nickel supported on nitrogen-doped carbon nanotubes as hydrogen oxidation reaction catalyst in alkaline electrolyte, *Nat. Commun.*, 2016, **7**(1), 10141, DOI: 10.1038/ncomms10141.

37 X. Bu, Z. Mao, Y. Bu, Q. Quan, Y. Meng, Z. Lai, D. Chen, P. Xie, H. Li, C. Liu, X. Wang, S. Yip, J. Lu and J. C. Ho, Remarkable gas bubble transport driven by capillary pressure in 3D printing-enabled anisotropic structures for efficient hydrogen evolution electrocatalysts, *Appl. Catal., B*, 2023, **320**, 121995, DOI: 10.1016/j.apcatb.2022.121995.

38 R. B. Patil, S. D. House, A. Mantri, J. C. Yang and J. R. McKone, Direct Observation of Ni–Mo Bimetallic Catalyst Formation *via* Thermal Reduction of Nickel Molybdate Nanorods, *ACS Catal.*, 2020, **10**(18), 10390, DOI: 10.1021/acscatal.0c02264.

39 L. Chen and A. Lasia, Ni–Al Powder Electrocatalyst for Hydrogen Evolution: Effect of Heat-Treatment on Morphology, Composition, and Kinetics, *J. Electrochem. Soc.*, 1993, **140**(9), 2464, DOI: 10.1149/1.2220845.

40 L. Chen and A. Lasia, Study of the Kinetics of Hydrogen Evolution Reaction on Nickel-Zinc Powder Electrodes, *J. Electrochem. Soc.*, 1992, **139**(11), 3214, DOI: 10.1149/1.2069055.

41 S. Wang, B. Hsia, C. Carraro and R. Maboudian, High-performance all solid-state micro-supercapacitor based on patterned photoresist-derived porous carbon electrodes and an ionogel electrolyte, *J. Mater. Chem. A*, 2014, **2**(21), 7997, DOI: 10.1039/C4TA00570H.

42 B.-A. Mei, J. Lau, T. Lin, S. H. Tolbert, B. S. Dunn and L. Pilon, Physical Interpretations of Electrochemical Impedance Spectroscopy of Redox Active Electrodes for Electrical Energy Storage, *J. Phys. Chem. C*, 2018, **122**(43), 24499, DOI: 10.1021/acs.jpcc.8b05241.

43 C. Hitz and A. Lasia, Experimental study and modeling of impedance of the her on porous Ni electrodes, *J. Electroanal. Chem.*, 2001, **500**(1), 213, DOI: 10.1016/S0022-0728(00)00317-X.

44 M. Wang, H. Yang, J. Shi, Y. Chen, Y. Zhou, L. Wang, S. Di, X. Zhao, J. Zhong, T. Cheng, W. Zhou and Y. Li, Alloying Nickel with Molybdenum Significantly Accelerates Alkaline Hydrogen Electrocatalysis, *Angew. Chem., Int. Ed.*, 2021, **60**(11), 5771, DOI: 10.1002/anie.202013047.

45 W. Zhang, J. Zheng, X. Gu, B. Tang, J. Li and X. Wang, Facile synthesis, characterization and DFT studies of a nanostructured nickel–molybdenum–phosphorous planar electrode as an active electrocatalyst for the hydrogen evolution reaction, *Nanoscale*, 2019, **11**(19), 9353, DOI: 10.1039/C8NR08039A.

46 J. Ekspong, N. Boulanger and E. Gracia-Espino, Surface activation of graphene nanoribbons for oxygen reduction reaction by nitrogen doping and defect engineering: an ab initio study, *Carbon*, 2018, **137**, 349, DOI: 10.1016/j.carbon.2018.05.050.

47 E. Gracia-Espino, Behind the Synergistic Effect Observed on Phosphorus–Nitrogen Codoped Graphene during the Oxygen Reduction Reaction, *J. Phys. Chem. C*, 2016, **120**(49), 27849, DOI: 10.1021/acs.jpcc.6b09425.

48 J. Wang, S. Xin, Y. Xiao, Z. Zhang, Z. Li, W. Zhang, C. Li, R. Bao, J. Peng, J. Yi and S. Chou, Manipulating the Water Dissociation Electrocatalytic Sites of Bimetallic Nickel-Based Alloys for Highly Efficient Alkaline Hydrogen Evolution, *Angew. Chem., Int. Ed.*, 2022, **61**(30), e202202518, DOI: 10.1002/anie.202202518.

49 A. Mohsenzadeh, K. Bolton and T. Richards, DFT study of the adsorption and dissociation of water on Ni(111), Ni(110) and Ni(100) surfaces, *Surf. Sci.*, 2014, **627**, 1, DOI: 10.1016/j.susc.2014.04.006.

50 R.-Q. Yao, Y.-T. Zhou, H. Shi, W.-B. Wan, Q.-H. Zhang, L. Gu, Y.-F. Zhu, Z. Wen, X.-Y. Lang and Q. Jiang, Nanoporous Surface High-Entropy Alloys as Highly Efficient Multisite Electrocatalysts for Nonacidic Hydrogen Evolution Reaction, *Adv. Funct. Mater.*, 2021, **31**(10), 2009613, DOI: 10.1002/adfm.202009613.

51 C.-W. Hu, Y. Yamada and K. Yoshimura, Fabrication of nickel oxyhydroxide/palladium (NiOOH/Pd) nanocomposite for gasochromic application, *Sol. Energy Mater. Sol. Cells*, 2018, **177**, 120, DOI: 10.1016/j.solmat.2017.01.021.

52 H. Jiang, Y. Guo, T. Wang, P.-L. Zhu, S. Yu, Y. Yu, X.-Z. Fu, R. Sun and C.-P. Wong, Electrochemical fabrication of $Ni(OH)_2$/Ni 3D porous composite films as integrated capacitive electrodes, *RSC Adv.*, 2015, **5**(17), 12931, DOI: 10.1039/C4RA15092A.

53 A. Nadeema, V. M. Dhavale and S. Kurungot, NiZn double hydroxide nanosheet-anchored nitrogen-doped graphene enriched with the γ-NiOOH phase as an activity modulated water oxidation electrocatalyst, *Nanoscale*, 2017, **9**(34), 12590, DOI: 10.1039/C7NR02225E.

54 A. De Jong, H. Borg, L. Van IJzendoorn, V. Soudant, V. De Beer, J. Van Veen and J. Niemantsverdriet, Sulfidation mechanism by molybdenum catalysts supported on silica/silicon (100) model support studied by surface spectroscopy, *J. Phys. Chem.*, 1993, **97**(24), 6477, DOI: 10.1021/j100126a024.

 This journal is © the Owner Societies 2023

Open Access Article. Published on 07 July 2023. Downloaded on 1/22/2026 5:08:32 PM.
This article is licensed under a Creative Commons Attribution 3.0 Unported Licence.

55 C. Lei, S. Lyu, J. Si, B. Yang, Z. Li, L. Lei, Z. Wen, G. Wu and Y. Hou, Nanostructured Carbon Based Heterogeneous Electrocatalysts for Oxygen Evolution Reaction in Alkaline Media, *ChemCatChem*, 2019, **11**(24), 5855, DOI: 10.1002/cctc.201901707.

56 J.-H. Park, J. C. Ro and S.-J. Suh, FeCo nanoparticles with different compositions as electrocatalysts for oxygen evolution reaction in alkaline solution, *Appl. Surf. Sci.*, 2022, **589**, 153041, DOI: 10.1016/j.apsusc.2022.153041.

57 P. Babar, A. Lokhande, V. Karade, B. Pawar, M. G. Gang, S. Pawar and J. H. Kim, Towards highly efficient and low-cost oxygen evolution reaction electrocatalysts: an effective method of electronic waste management by utilizing waste Cu cable wires, *J. Colloid Interface Sci.*, 2019, **537**, 43, DOI: 10.1016/j.jcis.2018.10.079.

58 A. Govind Rajan and E. A. Carter, Microkinetic model for pH- and potential-dependent oxygen evolution during water splitting on Fe-doped β-NiOOH, *Energy Environ. Sci.*, 2020, **13**(12), 4962, DOI: 10.1039/D0EE02292F.